Journal of Materials Science & Technology 189 (2024) 68–76

Contents lists available at ScienceDirect

Journal of Materials Science & Technology

journal homepage: www.elsevier.com/locate/jmst

Research Article

Stable switching behavior of low-temperature ZrO_2 RRAM devices realized by combustion synthesis-assisted photopatterning

Bongho Jang[a], Junil Kim[a], Jieun Lee[a], Jaewon Jang[b,c], Hyuk-Jun Kwon[a,d,*]

[a] Department of Electrical Engineering and Computer Science, DGIST, Daegu 42988, Korea
[b] School of Electronic and Electrical Engineering, Kyungpook National University, Daegu 41566, Korea
[c] School of Electronics Engineering, Kyungpook National University, Daegu 41566, Korea
[d] Convergence Research Advanced Centre for Olfaction, DGIST, Daegu 42988, Korea

ARTICLE INFO

Article history:
Received 9 September 2023
Revised 18 November 2023
Accepted 4 December 2023
Available online 17 January 2024

Keywords:
ZrO_2
Combustion
Sol-gel
RRAM
Patterning

ABSTRACT

We have realized efficient photopatterning and high-quality ZrO_2 films through combustion synthesis and manufactured resistive random access memory (RRAM) devices with excellent switching stability at low temperatures (250 °C) using these approaches. Combustion synthesis reduces the energy required for oxide conversion, thus accelerating the decomposition of organic ligands in the UV-exposed area, and promoting the formation of metal-oxygen networks, contributing to patterning. Thermal analysis confirmed a reduction in the conversion temperature of combustion precursors, and the prepared combustion ZrO_2 films exhibited a high proportion of metal-oxygen bonding that constitutes the oxide lattice, along with an amorphous phase. Furthermore, the synergistic effect of combustion synthesis and UV/O_3-assisted photochemical activation resulted in patterned ZrO_2 films forming even more complete metal-oxygen networks. RRAM devices fabricated with patterned ZrO_2 films using combustion synthesis exhibited excellent switching characteristics, including a narrow resistance distribution, endurance of 10^3 cycles, and retention for 10^5 s at 85 °C, despite low-temperature annealing. Combustion synthesis not only enables the formation of high-quality metal oxide films with low external energy but also facilitates improved photopatterning.

1. Introduction

In recent years, the rapid growth of data-intensive computing systems such as artificial intelligence (AI), big data analysis, and Internet of Things (IoT) devices has increased the demand for next-generation memory devices that offer better durability, faster operating speed, and higher energy efficiency [1–5]. Conventional memory technologies like flash memory have been widely used as the foundation of computing systems. However, with the advent of AI and IoT applications, these conventional memory devices are facing performance and scalability limitations due to the continuously increasing demands for data storage and processing [5–7]. As a result, alternative memory technologies have been proposed to address these challenges and meet the increasing data requirements. Resistive random access memory (RRAM) is gaining significant attention as one of the next-generation non-volatile memories due to its technological features, such as low power consumption, high operating speed, and excellent stability [8–10]. Moreover, these devices provide high scalability through a simple crossbar structure, enabling them to meet the increasing data requirements [4,11]. RRAM typically consists of a simple two-terminal capacitor structure with dielectric materials inserted between two electrodes. The memory characteristics of RRAM are determined by the properties of the dielectric materials, which act as the switching layer [12]. Accordingly, many studies have been conducted to find various materials (including organic, inorganic, and electrolytes) suitable for switching layers [13–15], along with efforts to implement high-quality switching layers to enhance memory characteristics [16–18]. Among them, metal oxides such as TiO_2, ZnO, NiO, WO_3, Cu_xO, and Al_2O_3 have been investigated as promising candidates for the switching layer due to their CMOS compatibility and wide bandgap, which provides optical transparency and low leakage current [19–21]. Especially, ZrO_2, with its high dielectric

* Corresponding author.
E-mail address: hj.kwon@dgist.ac.kr (H.-J. Kwon).

https://doi.org/10.1016/j.jmst.2023.12.016

constants (> 20) and excellent electrical/chemical reliability, has the potential to serve as the switching layer in low-voltage RRAM devices and can contribute to low-power operation, which is required for next-generation memories [22–24]. In various studies, ZrO_2-based RRAM devices have exhibited good switching characteristics [25–27], and it has also been reported that ZrO_2 can be used in a multilayer structure to control the switching behavior [28–30]. In addition, to implement an RRAM crossbar array instead of a single RRAM device, a selector is required to overcome the sneak path problem [31]. The ZrO_2 layer can be used not only as the switching layer in RRAM but also as the insulator layer in thin-film transistors that can serve as selectors [31–33]. This can reduce unnecessary process steps, saving both process time and cost.

From the process perspective, the fabrication of metal oxides for RRAM has been conducted using costly equipment and time-consuming vacuum systems (e.g., sputtering or atomic layer deposition) [34,35]. Furthermore, these methods are limited in the substrate area that can be deposited, depending on the volume of the vacuum chamber. These limitations have spurred the demand for new processing methods, and the sol-gel approach has emerged as a promising alternative for low-cost, large-area metal oxide electronic devices. Metal oxide films fabricated through the sol-gel approach are formed from liquid precursors, allowing for flexible control over the internal components of the precursor to obtain optimized oxide films. Furthermore, these precursors can be utilized as inks in solution-based techniques such as spin coating or printing, offering the advantages of simple and cost-effective deposition of metal oxide films on large areas [36–38]. However, there are challenges that need to be addressed to practically utilize these solution-based technologies.

First, a considerable amount of energy is required to convert the precursor into an oxide film and sufficiently remove internal organic residues, and for this, high-temperature annealing of > 400 °C is usually accompanied by precursor deposition. Previous reports on solution-processed ZrO_2 RRAM devices also included high-temperature post-annealing to obtain good switching characteristics, and low-temperature-processed devices had significantly reduced endurance and retention performance due to deteriorated oxide films [21,39]. Unfortunately, high-temperature processing affects adjacent regions and causes deformation to the heat-sensitive plastic substrates commonly used in flexible device development. Therefore, various techniques (such as UV photo annealing, O_2 annealing, and aqueous solvent) have been investigated to achieve sol-gel-based oxide films at low temperatures without compromising the quality of the films and satisfying thermal compatibility with plastic substrates [40–42]. Among them, combustion synthesis is one of the chemical approaches that enable the fabrication of various high-quality oxide films at low temperatures without the need for additional equipment [43]. Furthermore, it can be combined with other approaches to boost their effectiveness. The high-quality ZrO_2 films obtained through combustion processes at low temperatures can significantly enhance RRAM devices' switching characteristics, particularly the stability-related performance.

Another challenge is to develop alternative methods for patterning solution-processed oxide films. Until now, patterning technology has been developed based on photolithography. This technology enables accurate and fine pattern implementation, but the relatively complex process contrasts with the productivity of solution-based technologies. As a result, various patterning methods, such as printing techniques and surface energy modulation, have been studied [37,44,45]. Inkjet and gravure printing technologies have shown good compatibility with solution-based processes but have difficulties in uniformly controlling the shape, thickness, and morphology of patterns. Surface energy control also faces the challenge of nonuniform pattern formation caused by the coffee ring effect [46]. Achieving uniform pattern formation is a crucial issue directly linked to the performance of the RRAM device. In this regard, UV photopatterning using the photoreaction of solution-processed oxide films is proposed as a new alternative. Patterned films are created through selective precursor conversion in the UV-exposed areas using a shadow mask, and the precursor in the non-exposed regions is removed by rinsing with a developing solution. Unlike the techniques above, this method is one of the subtractive approaches that allow for fine patterning while ensuring the morphological uniformity of patterned films [47,48]. However, conventional sol-gel methods still face challenges in effective photopatterning through photoreaction due to the considerable energy required for the decomposition of organic ligands and conversion into oxide films. Combustion synthesis promotes oxide formation even at low external energy due to the chemical energy generated by the exothermic reaction [49], so the precursor conversion can be induced more effectively than conventional precursors during UV irradiation for photopatterning. Therefore, combustion synthesis can be a promising approach for manufacturing sol-gel-based oxide RRAM, as it simultaneously enables effective photopatterning and the formation of high-quality oxides at low temperatures. Despite these potential advantages, there are few reports on ZrO_2 RRAM devices that achieve both high-quality ZrO_2 film fabrication and effective patterning for the switching layers using combustion synthesis.

In this paper, we report the implementation of efficient photopatterning and high-quality ZrO_2 films through combustion synthesis, and the excellent switching stability of RRAM devices fabricated at low temperatures using these approaches. Photopatterning is distinguished from blocked regions through the selective precursor conversion in the UV-exposed areas. Combustion synthesis reduces the energy required for oxide conversion, thus accelerating the decomposition of organic ligands in the exposed area, and promoting the formation of metal-oxygen networks, contributing to patterning. We conducted thermogravimetric analysis (TGA) and confirmed a reduced temperature for the conversion to oxides by combustion synthesis. The structural properties and internal composition differences between ZrO_2 films fabricated from conventional and combustion precursors were investigated using grazing incidence X-ray diffraction (GIXRD) and X-ray photoelectron spectroscopy (XPS) spectra. The prepared combustion ZrO_2 films exhibited an amorphous phase with high metal-oxygen contents that constitute the lattice. Using combustion synthesis-based patterning and ZrO_2 films, we fabricated Ag/ZrO_2/ITO structured RRAM devices at low temperatures (250 °C) and evaluated their switching behavior. The prepared RRAM devices demonstrated excellent switching characteristics, including a narrow resistance distribution, endurance of 10^3 cycles, and retention for 10^5 s at 85 °C.

2. Experimental methods

2.1. Synthesis of combustion ZrO_2 solution

ZrO_2 solutions were prepared through the following process. First, 0.001 mol of Zirconium acetylacetonate ($Zr(C_5H_7O_2)_4$) was dissolved in 10 mL of ethanol for 0.1 M zirconium solution. Then, the prepared solution was subjected to ultrasonication for 1 h to obtain a clear answer. Next, 0.001 mol of ammonium nitrate (NH_4NO_3) and urea ($CO(NH_2)_2$), which act as the oxidizer and fuel in the combustion solution, were added to the zirconium solution. Fig. S1(a) in the Supplementary material illustrates the chemical reactions associated with combustion synthesis. In the basic mechanism of combustion synthesis, the fuels ignite at low external energy to provide chemical energy inside, and NO_3^- acts as an oxidizer, effectively aiding in the combustion reaction, which is a type of redox reaction. For the Zr source we used, it did not contain oxidizers in the anion, so we used NH_4NO_3 as a substance to pro-

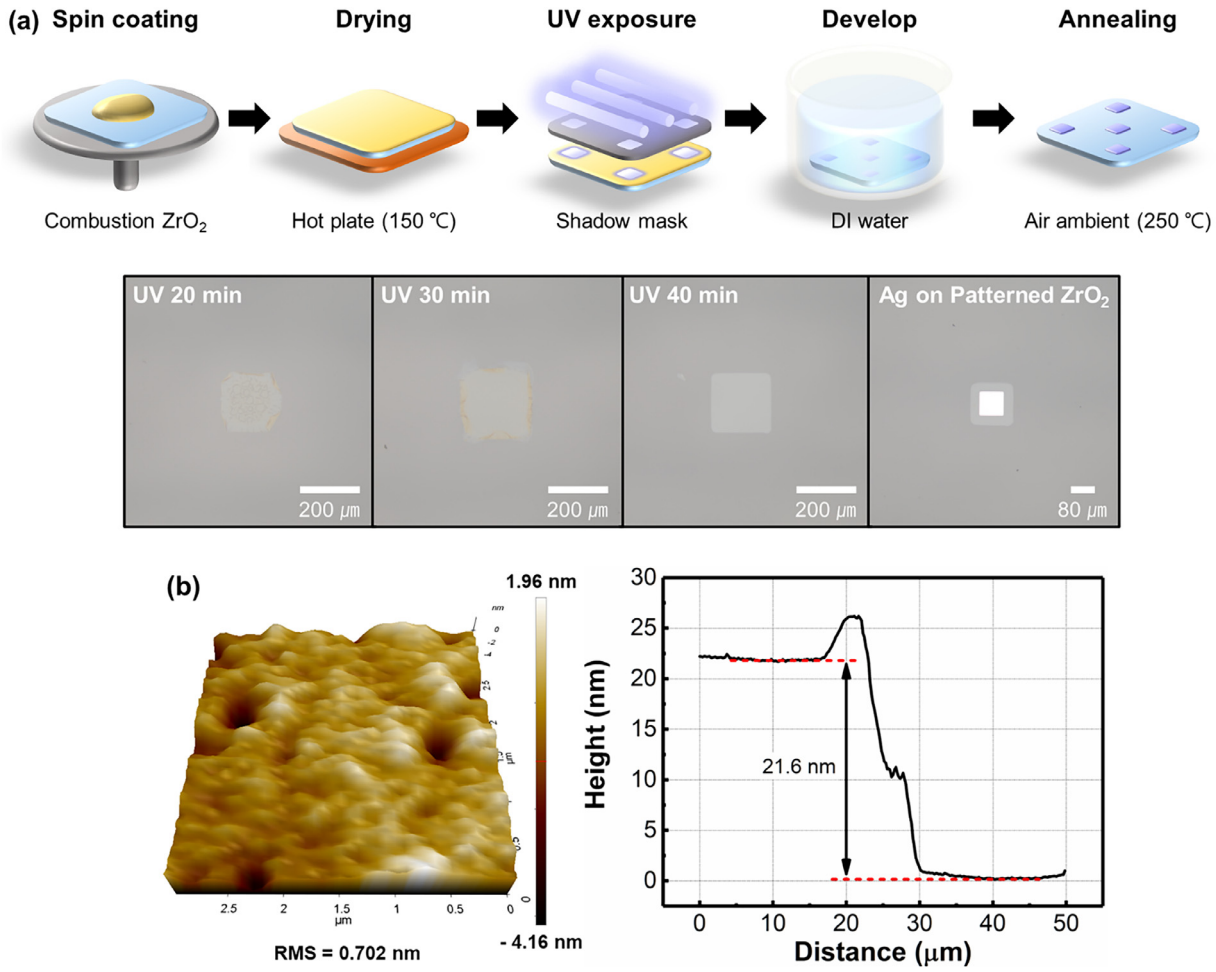

Fig. 1. (a) Schematics of ZrO_2 films photopatterning based on combustion synthesis, and optical images of patterned ZrO_2 films for various UV exposure times. (b) AFM images of patterned films and thickness obtained through step measurements.

vide NO_3^-, and finally, we added $CO(NH_2)_2$ as the fuel for ignition. The mixture was aged at 80 °C for 48 h, resulting in a clear yellowish solution. Conventional precursors were prepared using only $Zr(C_5H_7O_2)_4$ without adding an oxidizer and fuel used in combustion precursors.

2.2. Fabrication process of ZrO_2 rram

The prepared ZrO_2 solutions were spin-coated on indium tin oxide (ITO)-coated glass substrates to form the ITO/ZrO_2 structure. Before coating, the ITO-coated glass was subjected to UV/O_3 treatment for 10 min to control its wettability. The prepared solutions were spin-coated on ITO-coated glass at 3000 rpm for 50 s and dried on a hot plate heated to 150 °C for 1 min. To pattern the ZrO_2 films deposited on the front surface of ITO, a shadow mask was placed over the dried ZrO_2 films, and UV exposure was performed for various durations using UV/O_3 equipment. Afterward, the UV-treated ZrO_2 films were developed in DI water for 1 min. The schematics of the preparation steps for ZrO_2 RRAM are shown in Fig. 1, and the results of ZrO_2 patterning with respect to UV exposure time will be addressed below. The UV light used for patterning has two main wavelengths: 254 and 184 nm, with an intensity of 28 mW cm^{-2}. The patterned ZrO_2 films were annealed at a low temperature of 250 °C for 1 h to induce thermal activation. Lastly, 50 nm-thick Ag electrodes (80 μm × 80 μm) were deposited onto the patterned ZrO_2 films using thermal evaporators, resulting in the fabrication of Ag/ZrO_2/ITO structured RRAM devices.

2.3. Characterization of ZrO_2 films and RRAM

TGA was utilized for the thermal behavior analysis of the prepared combustion precursors. The thermal behavior of the dried precursors was monitored while heating them at a rate of 10 °C/min. The changes in the structural properties of the prepared ZrO_2 films were observed through GIXRD with Cu Kα radiation (λ = 1.54 Å). The film surface morphology and the thickness of patterned ZrO_2 films were determined using atomic force microscopy (AFM). The internal compositional changes of the ZrO_2 films fabricated using conventional and combustion precursors were analyzed using XPS with a monochromatic Al Kα (1488 eV) source. The switching characteristics of Ag/ZrO_2/ITO RRAM were measured using a Keithley 4200-SCS analysis system at a probe station.

3. Results and discussion

Fig. 1(a) illustrates the process of patterning ZrO_2 film for manufacturing RRAM and exhibits the varying ZrO_2 patterns on an ITO substrate according to the UV exposure time. UV irradiation of metal precursors induces photolytic decomposition of ligands and partial metal-oxygen bonding, leading to differences in the films compared to the unexposed areas [40]. The photopatterning of combustion precursors compared to conventional precursors following the described steps can be observed in Fig. S1(b, c). When exposed to UV light for the same duration on Si sub-

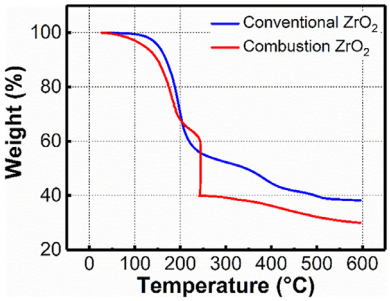

Fig. 2. TGA results of the combustion and conventional ZrO_2 precursors.

strates, the combustion ZrO_2 films clearly separate between the exposed and unexposed areas, and only the areas exposed to UV after the development are patterned. In contrast, conventional ZrO_2 patterns exhibit messy boundaries, which is due to the inadequate rinsing of the areas blocked by the shadow mask with not only DI water but also ethanol during the developing process, revealing the limitations in photopatterning of conventional precursors. Such differences arise due to the reduced energy required for the conversion into oxides through combustion synthesis, which facilitates sufficient precursor decomposition and accelerates the formation of metal-oxygen networks upon UV exposure. After verifying the patterning effect of combustion precursors, we controlled the UV exposure time to obtain clear ZrO_2 patterns for the Ag/ZrO_2/ITO structure. Short-duration UV exposure (20 min) fails to induce sufficient decomposition of the ligands, resulting in unclear and rounded boundaries. The surface of the UV-exposed ZrO_2 films appears to be rough and not smooth. However, as the UV exposure time increases, the boundaries of the patterns become progressively clearer, and optimal ZrO_2 patterns are obtained with 40 min of UV treatment. The surface morphology of the patterned ZrO_2 films is shown in Fig. 1(b), and the RMS roughness of the films is estimated to be 0.702 nm, indicating smooth surface characteristics. Also, the thickness of the ZrO_2 films obtained by step measurement using AFM is 21.6 nm. We fabricated RRAM devices by depositing Ag top electrodes onto clearly patterned ZrO_2 films. In addition, the UV process conducted using UV/O_3 equipment can observe other effects besides patterning. UV reacts with oxygen in the air to generate O_3 and oxygen radicals. Due to their high diffusivity and reactivity compared to oxygen, the generated oxygen radicals can promote the formation of metal-oxygen bonds even at low temperatures and play a role in removing organic residues [50]. This can create a synergistic effect by combining with the low-temperature process, which is the combustion synthesis we used. The compositional changes of the ZrO_2 films caused by UV/O_3 treatment will be further investigated in detail in the XPS spectra below.

Fig. 2 shows the TGA curves of different ZrO_2 precursors, which were measured to estimate the energy required for precursor conversion. The conversion is determined based on the temperature range in the TGA curves where weight change is observed. The weight of the combustion precursors abruptly decreases by more than 20% at around 240 °C, and after that, the weight change is relatively insignificant. In contrast, the conventional precursors exhibit similar curves below 200 °C but show a gradual weight loss without any noticeable changes. Therefore, based on the TGA curves, it can be observed that combustion precursors undergo most of the conversion at around 240 °C, whereas conventional precursors require temperatures above 400 °C. TGA analysis suggests that the precursor conversion temperature in the combustion system occurs at a notably lower temperature than conventional precursors. This difference in conversion temperature indicates that the external energy required for conversion to oxide is reduced due to the internal energy generated by the exothermic reaction of the combustion precursors. Based on the conversion temperature obtained from thermal analysis, we determined that sufficient conversion into ZrO_2 films could occur even at 250 °C. Also, we anticipate that the fabricated ZrO_2 RRAM devices exhibit improved performance compared to devices manufactured using conventional precursors that require high-temperature annealing. Details about these expected outcomes will be discussed further in the subsequent section on electrical characteristics.

The structural properties of the oxide films used as the switching layers significantly influence the switching properties of the prepared RRAM. In crystalline oxides, the grain boundaries are the sites where oxygen vacancies or metal cations migrate, providing paths for the formation of conductive filaments [51–53]. Furthermore, randomly distributed grain boundaries can lead to fluctuations in the switching behavior, associated with non-uniform forming voltages and reset operations, and contribute to an increase in leakage current [51,54]. Fig. 3 represents the GIXRD spectra of prepared ZrO_2 films to analyze structural properties. All ZrO_2 films exhibit minor peaks corresponding to the monoclinic structure in the range of 50° to 60°. The spectra of the combustion ZrO_2 films with UV exposure for patterning and subsequent annealing at 250 °C show an amorphous state without distinct peaks. In contrast, ZrO_2 films annealed at 400 °C using conventional precursors exhibit diffraction peaks at 30.5°, 35.2°, 50.7°, and 60.3° corresponding to the (111), (200), (220), and (311) planes, respectively, which match the cubic structure of ZrO_2 films (JCPDS No. 27–0997). Additionally, they reveal a polycrystalline structure, distinct from other films, with distinct peaks. The ZrO_2 films annealed at 250 °C, regardless of the precursor type, disclose an amorphous state without clear peaks, indicating that low-temperature annealing makes it challenging for ZrO_2 crystalline growth. Considering these results, combustion ZrO_2 films with an amorphous structure can contribute to mitigating the instability of RRAM switching behavior related to structural properties when compared to crystalline ZrO_2 films obtained through high-temperature annealing.

We investigated the internal composition changes of the ZrO_2 films fabricated using different precursors through XPS analysis. The O 1s spectra of ZrO_2 films prepared under various conditions are shown in Fig. 4. These spectra have been deconvoluted into peaks corresponding to metal-oxygen bonding (M–O) at 529.9 eV, oxygen vacancy (V_o) at 531.3 eV, and metal hydroxide (M–OH) at 532.2 eV, respectively [55,56]. The calculated area ratios of the three O 1s subpeaks are summarized in Fig. 4(e). Unlike M–O, which represents a metal-oxygen network in ZrO_2 films, OH groups are intermediate products formed during precursor conversion. They can serve as oxygen-associated trap sites, and the presence of both low M–O and high M–OH contents indicates the formation of an incomplete oxide network. Additionally, oxygen vacancies play a significant role in the filament formation of RRAM devices. They can constitute filaments on their own, and in electrochemical metallization (ECM)-type devices, they can act as pathways that enhance the diffusion of metal ions [29,57,58]. ZrO_2 films annealed at 250 °C through combustion synthesis exhibit higher M–O content and reduced V_o and M–OH contents compared to the conventional ZrO_2 films annealed at 400 °C. These differences suggest that combustion ZrO_2 films form a relatively complete oxide lattice even with low-temperature annealing. This is attributed to the chemical energy generated from combustion precursors, which enables precursor conversion and lattice formation at lower temperatures. Furthermore, these results are consistent with the previous TGA analysis, which showed that most of the precursor conversion was completed at around 240 °C, in contrast to conventional systems requiring high temperatures. After UV irradiation for patterning, the combustion ZrO_2 films still exhibit low M–O content and high V_o and M–OH content compared

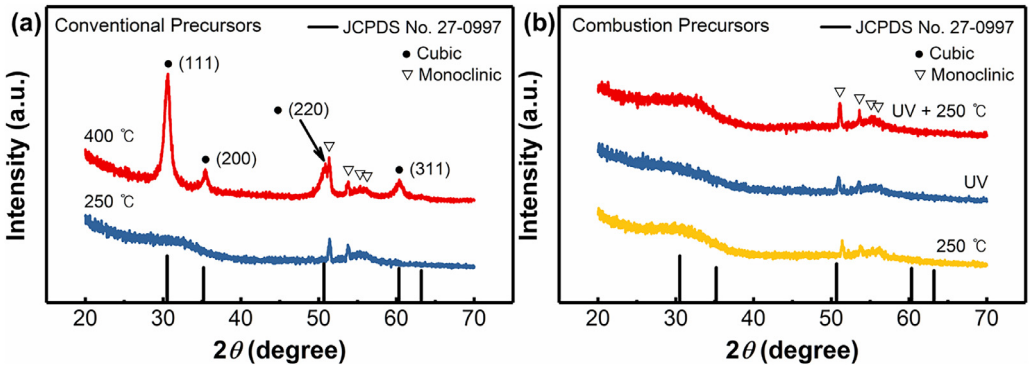

Fig. 3. (a) GIXRD spectra of the (b) Conventional and (b) Combustion ZrO_2 films annealed under different conditions.

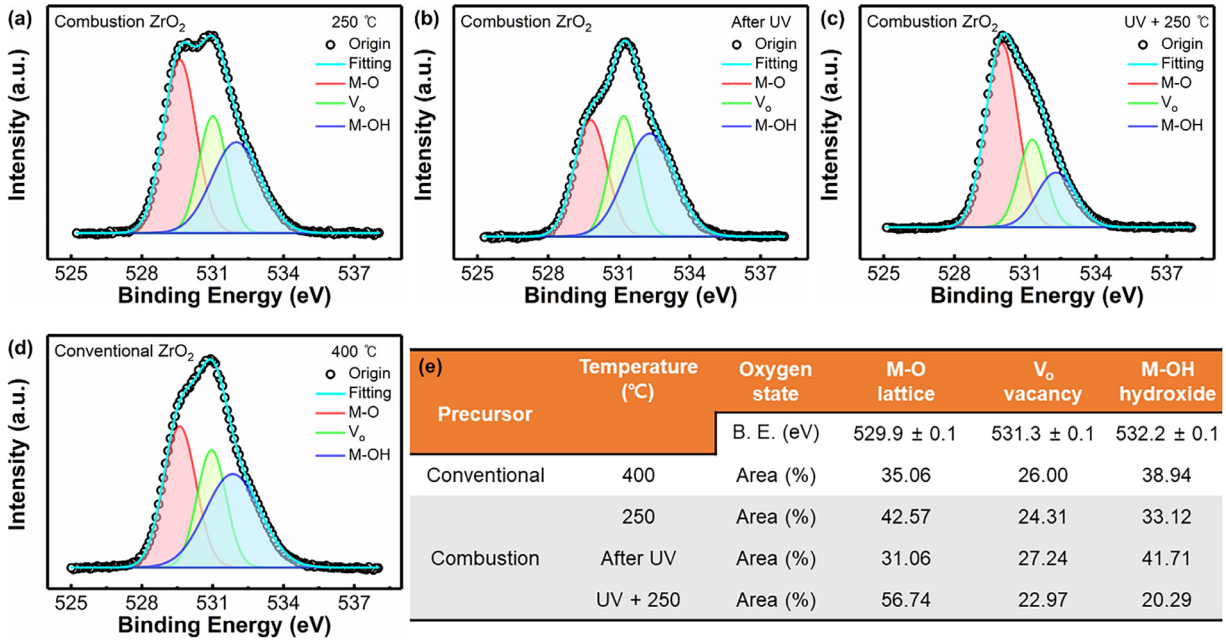

(e) Precursor	Temperature (℃)	Oxygen state	M-O lattice	V_o vacancy	M-OH hydroxide
		B. E. (eV)	529.9 ± 0.1	531.3 ± 0.1	532.2 ± 0.1
Conventional	400	Area (%)	35.06	26.00	38.94
Combustion	250	Area (%)	42.57	24.31	33.12
	After UV	Area (%)	31.06	27.24	41.71
	UV + 250	Area (%)	56.74	22.97	20.29

Fig. 4. XPS O 1s spectra of the (a–c) Combustion and (d) Conventional ZrO_2 films annealed under different conditions. (e) Internal oxygen composition of ZrO_2 films prepared with different precursors and annealing processes.

to the annealed sample, which means that UV irradiation alone is not enough to construct sufficiently mature oxide lattices. However, the annealed samples show different oxygen compositions depending on whether UV exposure was performed. The M–O ratio of combustion ZrO_2 films annealed with UV exposure increases from 42.57% to 56.74%, while the V_o and M–OH ratios decrease. We would like to note that UV/O_3-assisted photochemical activation also contributes to ligand decomposition and metal-oxygen bonding during the film formation step. The highly diffusive and reactive oxygen radicals generated can promote metal-oxygen bonding even at low temperatures, leading to the formation of a more complete oxide network. This method provides uniform patterning of oxide films while facilitating metal oxide formation without a high-temperature process, similar to combustion synthesis. Therefore, through XPS analyses, it is demonstrated that the combustion system forms a more complete metal oxide network even at low temperatures with fewer oxygen-related defects (such as oxygen vacancies), and the combustion ZrO_2 films annealed after UV exposure exhibits high-quality films with enhanced metal-oxygen bonding. This serves as an example of the synergistic effect combined with combustion synthesis.

To investigate the effects of combustion synthesis on electrical performance, we fabricated Ag/ZrO_2/ITO RRAM devices and evaluated their switching characteristics. Our structures are based on the RRAM devices employing the ECM mechanism, similar to our previous report [21,56]. This structure operates as devices based on the movement of Ag ions and the associated oxidation and reduction reactions. By applying positive biases to the Ag top electrodes, Ag^+ ions generated as a result of oxidation at the Ag/ZrO_2 interface drift along the electric fields towards the bottom electrodes and undergo reduction to Ag atoms at the ZrO_2/ITO interface. These processes repeat, leading to the connection of conductive filaments within the switching layer. On the other hand, when negative biases are applied to the top electrodes, the Ag atoms constituting the filament are oxidized, causing them to return to the top electrode. This results in the breaking of the pathway connecting the electrodes, leading to restricted current flow. Fig. S2(a) shows the forming voltages of RRAM devices as a function of the number of ZrO_2 layers. As we increased the spin-coating cycles to increase the thickness of the ZrO_2 layer, higher forming voltages of over 10 V were required. Usually, a thicker switching layer requires higher forming voltages, which can be disadvantageous for low-power operations and may be more vulnerable to programming failures [59]. On the other hand, we confirmed in our previous research that reducing the thickness of the switching layer leads to a decrease in the high resistance state/low resistance state

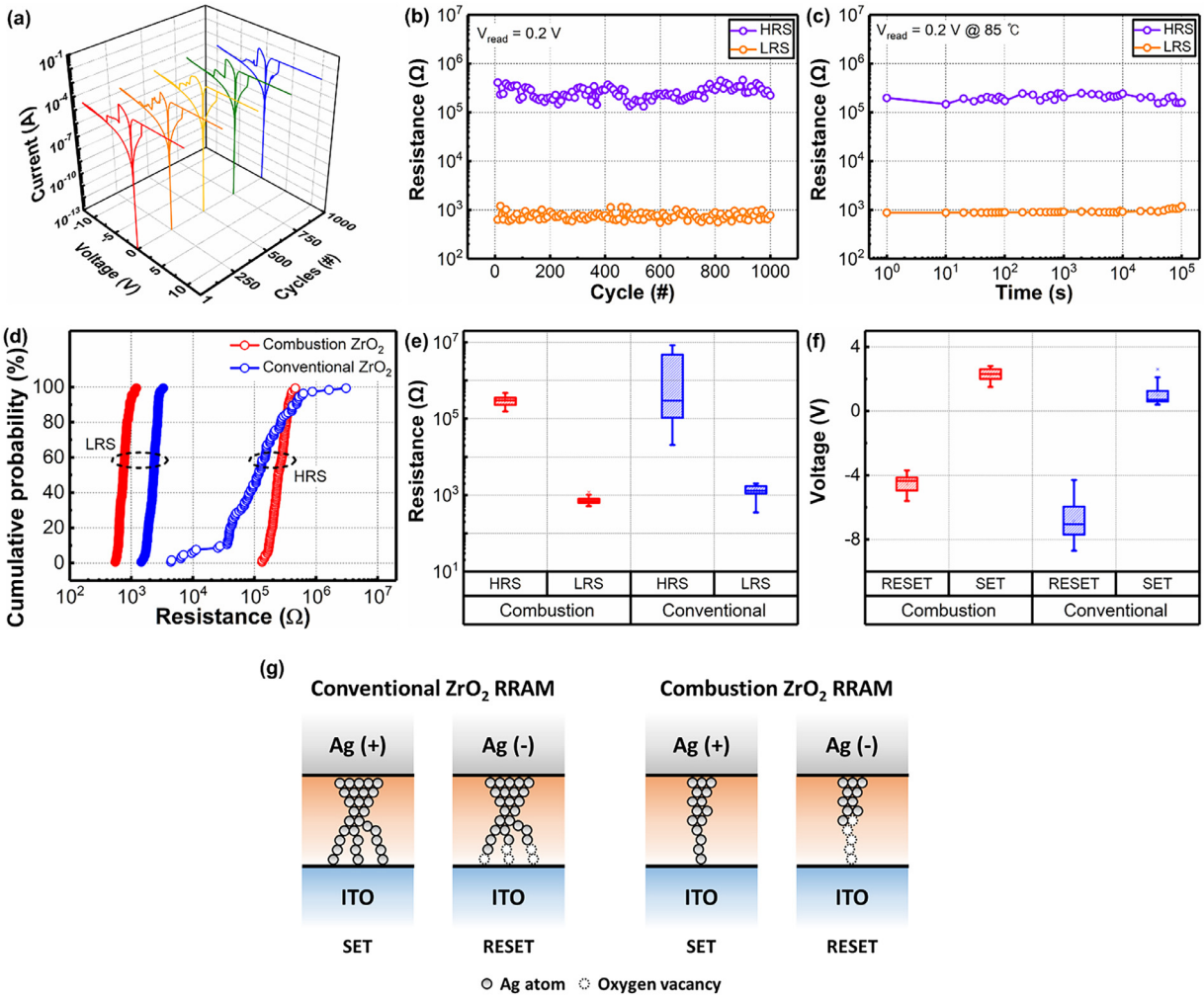

Fig. 5. Electrical characteristics of RRAM devices fabricated with patterned ZrO_2 films using combustion synthesis. (a) *I–V* curves obtained from continuous switching. (b) Endurance, and (c) Retention properties measured at a V_{read} of 0.2 V. (d) Cumulative probability distribution of resistances for patterned combustion and conventional ZrO_2 RRAM devices. Distribution of (e) resistance values and (f) V_{SET}/V_{RESET} for patterned combustion and conventional ZrO_2 RRAM devices. (g) Schematics of the process of filament formation and rupture in conventional and combustion RRAMs.

(HRS/LRS) ratio due to reduced HRS resistance [21]. Therefore, considering these factors, we chose a single-layer coating, specifically a 21.6 nm-thick ZrO_2 film, as the optimal thickness. Fig. 5 shows the switching characteristics of patterned ZrO_2 RRAMs using combustion precursors. In Fig. 5(a), these devices exhibit bipolar RRAM behavior, performing SET operation with abrupt resistance transition from a HRS to a LRS at a SET voltage (V_{SET}) of ~ 2.2 V, and executing RESET operation by returning to the HRS state at a RESET voltage (V_{RESET}) of ~ −4.7 V. Also, the *I–V* curves of the combustion ZrO_2 RRAM show high switching repeatability, and the distribution of V_{SET}/V_{RESET} extracted at 10 intervals at 1000 cycles is shown in Fig. S3. The endurance and retention characteristics, which depict the switching repeatability of the fabricated ZrO_2 RRAM, are presented in Fig. 5(b, c). The resistance values at the HRS/LRS state for endurance and retention characteristics are extracted at a read voltage of + 0.2 V. These figures reveal that the fabricated devices exhibit stable switching behavior. The HRS and LRS resistance values do not show any significant degradation even after 10^3 consecutive switching cycles, and retention, an essential characteristic of non-volatile memory, is maintained without noticeable fluctuation for 10^5 s at 85 °C. In many previous studies, resistance state changes were observed for > 10^4 s at an elevated temperature of 85 °C, allowing for simple predictions of retention times [60–63]. When no significant changes were observed during the given monitoring period, retention times were extrapolated to be over 10 years. The patterned ZrO_2 RRAMs showed no noticeable resistance changes for 10^5 s at 85 °C, demonstrating excellent data storage capabilities even at high temperatures. Also, this suggests that they are estimated to retain their data continuously for 10 years. These switching operations are clearly distinguished from the ZrO_2 RRAMs prepared with conventional precursors or only combustion precursors without patterning, as shown in Fig. S4. Conventional ZrO_2 RRAM annealed at 250 °C shows poor switching repeatability, with little window observed at 20 cycles. Devices annealed at 400 °C exhibit improved switching characteristics, but a continuously decreasing HRS/LRS ratio can be seen in the measured endurance along with apparent fluctuation in the resistance. Fig. S4(d, e) shows the switching characteristics of the ZrO_2 RRAM devices fabricated solely by combustion synthesis, without photopatterning. The prepared devices demonstrate improved switching repeatability compared to conventional ZrO_2 RRAMs, but there is observed fluctuation in resistance values, particularly in the HRS, in the endurance characteristics. Fig. 5(d) shows the cumulative distribution of HRS/LRS resistance values obtained from ZrO_2 RRAM fabricated with different precursors. These results demonstrate that combustion ZrO_2 RRAMs exhibit a higher HRS/LRS ratio and narrower resistance distribution compared to conventional devices annealed at high temperatures, indicating better uniformity

in switching behavior. The broad resistance distribution in conventional ZrO_2 RRAM can arise from the random formation and rupture of Ag conductive filaments [64]. Fig. 5(e, f) shows the statistical distributions of resistance values and V_{SET}/V_{RESET} among the fabricated RRAM devices. These results are based on measurements of more than 20 devices. The combustion ZrO_2 RRAMs exhibit much more uniform distributions compared to the conventional devices, with the difference particularly pronounced in the resistance values of the HRS. Furthermore, conventional ZrO_2 RRAMs exhibit higher V_{RESET} and lower V_{SET} compared to combustion RRAM devices. From the GIXRD spectra, we confirmed that the conventional ZrO_2 films annealed at high temperatures are in a polycrystalline phase, whereas the patterned combustion ZrO_2 films are composed of an amorphous phase. As mentioned earlier, fluctuations in the switching behavior associated with grain boundaries can be suppressed due to the amorphous phase. While the conventional ZrO_2 RRAM with polycrystalline phases shows widely distributed resistance states due to randomly conductive path formed along grain boundaries, the combustion ZrO_2 RRAM devices with amorphous phases, demonstrating narrow resistance distributions along with excellent switching stability, serve as evidence to support this. Oxygen-related defects within the switching layer also contribute to the degradation of the HRS, thereby causing instability in the switching behavior [58]. As oxygen-related defects like oxygen vacancies increase within our structure, the diffusion of Ag^+ ions is facilitated, leading to the creation of numerous conductive filament clusters. These increased clusters elevate leakage current, make filament breaking more challenging, leading to the irregularity of HRS resistance values, and consequently deteriorate endurance characteristics. Moreover, entrance into the LRS becomes easier while returning to the HRS becomes more difficult, causing a decrease in V_{SET} and an increase in V_{RESET}. The difference in the formation and rupture of filament clusters in conventional and combustion RRAMs is depicted in Fig. 5(g). The chemical energy generated by the exothermic reaction of the combustion precursors and the photochemical reaction induced by UV/O_3 treatment acted simultaneously to decompose alkoxide species and activate metal-oxygen bonding effectively. As a result, it can be observed from XPS spectra that the combustion ZrO_2 films annealed at 250 °C after UV exposure show a significant reduction in the content of V_o and M–OH groups, in comparison to the conventional ZrO_2 films annealed at high temperatures. This indicates the formation of high-quality ZrO_2 films, and the combustion of ZrO_2 RRAM can exhibit improved endurance characteristics as the formation of filament clusters is suppressed due to lower oxygen defects, leading to easier filament control. Therefore, photopatterned ZrO_2 RRAM devices with combustion synthesis exhibit stable switching behavior without noticeable degradation in the HRS even after multiple cycles of sweeping. This provides a clear contrast with the conventional ZrO_2 RRAM, where a distinct decrease in HRS was observed during 100 cycles of sweeping. Furthermore, compared to the conventional devices, the decrease in filament clusters resulting in the increased V_{SET} and decreased V_{RESET} can be distinctly observed in combustion ZrO_2 RRAM. The combustion ZrO_2 films fabricated without photopatterning also possess an immature metal oxide network with high V_o and M–OH groups compared to photopatterned ZrO_2 films. The relatively high levels of oxygen-related defects lead to switching instability, particularly contributing to the degradation of HRS. By combining the above factors, photopatterned ZrO_2 RRAMs with combustion synthesis exhibit improved switching behavior compared to conventional ZrO_2 devices annealed at high temperatures.

Additionally, we investigated the impact of device size on performance. Devices with relatively large areas tend to have a higher quantity of defects within the memory region, which can lead to the generation of more conductive filament clusters [65]. Fig. S2(b) depicts the switching characteristics of RRAM devices fabricated with different electrode areas. While no significant differences are observed in the overall switching behavior, a decrease in HRS is observed in the device with the largest electrode (120 μm × 120 μm). This is likely due to the increased filament clusters resulting from the larger memory area. However, the two devices of different sizes (60 μm × 60 μm, 80 μm × 80 μm) did not show significant differences. If the electrode areas of the devices are further reduced, an improvement in HRS can be expected due to the reduction of defects within the memory region. Also, V_{SET} and V_{RESET} in RRAM devices are correlated with the area and thickness of the devices. Devices with smaller areas contain fewer defects inducing filament formation in the memory region, resulting in a reduced V_{RESET} required to break the filaments. Additionally, previous studies have confirmed that a decrease in the thickness of the switching layer leads to a decrease in the V_{RESET} [21]. Therefore, appropriately controlling the device area and the thickness of the switching layer can be a method to reduce operating voltages. Furthermore, using electrodes structured in pyramid or nanocone shapes can effectively reduce the operation voltages [66,67]. Unlike planar electrodes, electric fields concentrated at the tips induce filaments only at the tips, achieving low V_{SET} and V_{RESET} with narrow distribution.

To clarify the working mechanism of the prepared ZrO_2 RRAM, we fabricated $Au/ZrO_2/ITO$ structures with inert Au as the top electrode and investigated their electrical characteristics. Fig. S4(f) shows the switching behavior of $Au/ZrO_2/ITO$ devices fabricated using combustion synthesis. Unlike the Ag electrode devices, the $Au/ZrO_2/ITO$ structures exhibit a narrow memory window and show unclear switching behavior. In contrast to the $Ag/ZrO_2/ITO$ structures, inert Au electrode devices do not follow the ECM mechanism, which involves the diffusion of metal ions generated by oxidation at the top electrodes to form filaments. Instead, they can operate as valence change memory (VCM) with filaments composed of oxygen vacancies. Unlike active metals like Al or Ti, Au does not act as a material that absorbs oxygen, making it difficult to induce oxygen vacancies at the Au/ZrO_2 interface, and this limits control over the distribution of oxygen vacancies within the ZrO_2 switching layer and leads to deteriorated switching behavior [68,69]. Therefore, the $Au/ZrO_2/ITO$ structures exhibit poor switching behavior compared to devices with Ag electrodes. Also, filament formation in VCM-type devices is also influenced by the work function difference between the top and bottom electrodes. The increased difference in work functions between the two electrodes further enhances filament formation [70,71]. In the previous report, when the Au (5.1 eV) electrodes were replaced with Pt (5.65 eV), which has a higher work function, clear switching behavior was observed [71]. This is attributed to the localized paths supplied by the work function difference, which play a crucial role in establishing conductive filaments based on oxygen vacancies [72].

To elucidate the details of the transport mechanism in photopatterned ZrO_2 RRAM, the scale of the IV curves was rescaled and is shown in Fig. 6. As seen in Fig. 6(a, b), in both the SET and RESET processes, the slope of the LRS state in ln scale is ~ 1, indicating ohmic conduction following the formation of conductive filaments. For the HRS state, it has been reported in the previous $Ag/ZrO_2/ITO$ structure that Poole-Frenkel emission is followed [21,56]. Poole-Frenkel emission is a mechanism in which thermally excited electrons within the conduction band of dielectric films overcome energy barriers and move between trap sites. The trap sites associated with conduction involve oxygen-related species or oxygen vacancies present within the oxide [73]. To verify whether this emission is matched, linear fitting was attempted on $\ln(I/V)$ vs. $V^{0.5}$, and the results are shown in Fig. 6(c, d). During the SET process, the HRS state exhibits a good fit to the Poole-

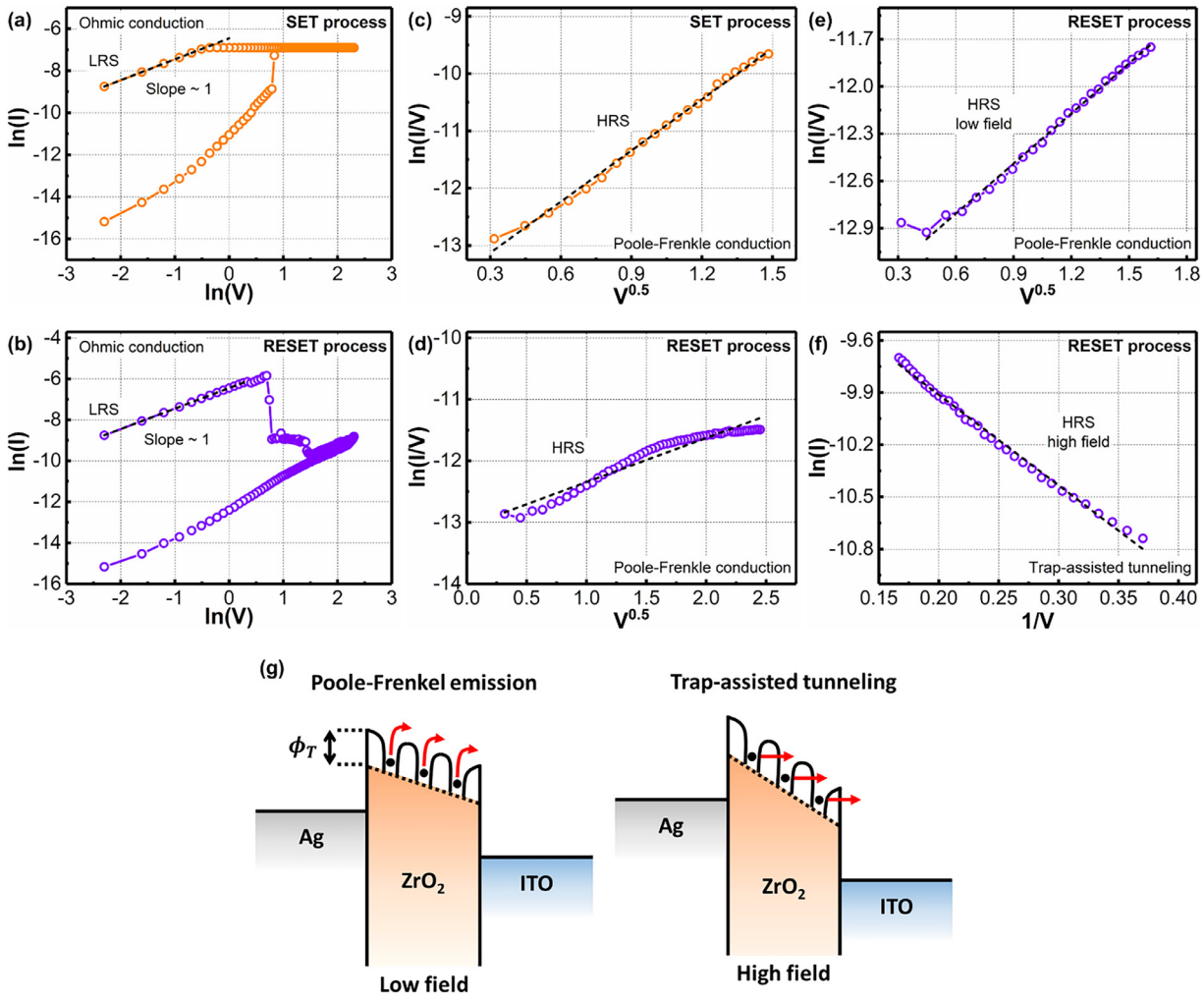

Fig. 6. Rescaled *I–V* curves for analyzing the conduction mechanism. *I–V* curves in the (a) SET and (b) RESET process adjusted on a ln-ln scale. *I–V* curves in the HRS during the (c) SET and (d) RESET processes adjusted to ln(*I*/*V*) vs. $V^{0.5}$. Conduction mechanisms dividing into (e) Poole-Frenkel conduction and (f) Trap-assisted tunneling based on the electric field in the HRS during the RESET process. (g) Schematics of the band diagram in the HRS during the RESET process under low/high electric field.

Frenkel fitting across the entire range. In contrast, during the RESET process, it shows partial agreement only in specific regions and exhibits different fittings depending on the electric field. The HRS *I–V* curves of the RESET process were fitted separately into the low field and high field, as shown in Fig. 6(e, f), and they are revealed to follow Poole-Frenkel and trap-assisted tunneling, respectively. Fig. 6(g) shows the schematics of the band diagram in the HRS state under low/high fields. This dual mechanism suggests that electrons conducting by overcoming trap-induced potential barriers at low electric fields undergo a transition to a conduction mechanism involving tunneling from trap sites to the bottom electrode as bias increases. Also, this phenomenon can only be observed in the RESET process because the lower V_{SET} compared to the V_{RESET} causes a transition to the LRS state before entering the high electric field required for tunneling.

4. Conclusions

In this paper, we have simultaneously achieved enhanced photopatterning and high-quality ZrO_2 films through combustion synthesis. Furthermore, utilizing these approaches, we fabricated ZrO_2 RRAM devices with stable switching behavior at low temperatures. Combustion synthesis involves the internal energy generated by exothermic reactions of combustion materials, allowing for the conversion to oxides even at low external temperatures. As a result, during photopatterning, the UV-exposed region's organic ligand decomposition and the formation of metal-oxygen bonding are facilitated, thus enhancing the effects of patterning. The TGA and GIXRD analyses demonstrated a reduction in the temperature required for the oxide conversion of combustion precursors and revealed that the combustion ZrO_2 films possess an amorphous crystalline structure. Furthermore, the O 1s spectra showed a high proportion of metal-oxygen bonding corresponding to the oxide lattice in the combustion ZrO_2 films. When exposed to UV light for photopatterning, they were confirmed to have formed even more complete metal-oxygen networks. This is attributed to the synergistic effect of combustion synthesis and UV/O_3-assisted photochemical activation, as it also contributes to ligand decomposition and metal-oxygen bonding during the film formation step. RRAM devices fabricated using combustion synthesis-based patterning and ZrO_2 films exhibited excellent switching characteristics, including a narrow resistance distribution, endurance of 10^3 switching cycles, and retention for 10^5 s at 85 °C, despite low-temperature annealing (250 °C). The improved switching stability is associated with the amorphous phase and the formation of a complete metal-oxygen network of the combustion ZrO_2 films. These factors contribute to the suppression of fluctuations in switching characteristics related to grain boundaries and the HRS degradation caused by oxygen-related defects. Combustion synthesis not only enables the formation of high-quality metal oxide films with low external energy

but also facilitates improved photopatterning. Therefore, this can be employed as a suitable process for the mass production of sol-gel process-based metal oxide electronic and flexible devices.

Declaration of competing interest

The authors declare that they have no known competing financial interests or personal relationships that could have appeared to influence the work reported in this paper.

Acknowledgments

This work was supported by the National Research Foundation of Korea (NRF) grants funded by the Ministry of Science and ICT (MSIT) (Nos. RS-2023–00251283, RS-2023–00257003, and 2022M3D1A2083618). Also, this work was supported by the DGIST R&D Program of the MSIT (No. 23-CoE-BT-03).

Supplementary materials

Supplementary material associated with this article can be found, in the online version, at doi:10.1016/j.jmst.2023.12.016.

References

[1] J.Q. Yang, Y. Zhou, S.T. Han, Adv. Electron. Mater. 7 (2021) 2001181.
[2] B.C. Jang, S. Kim, S.Y. Yang, J. Park, J.-H. Cha, J. Oh, J. Choi, S.G. Im, V.P. Dravid, S.-Y. Choi, Nano Lett. 19 (2019) 839–849.
[3] S. Bertolazzi, P. Bondavalli, S. Roche, T. San, S.Y. Choi, L. Colombo, F. Bonaccorso, P. Samorì, Adv. Mater. 31 (2019) 1806663.
[4] S.K. Vishwanath, J. Kim, J. Mater. Chem. C 4 (2016) 10967–10972.
[5] X. Wang, W. Xie, J.B. Xu, Adv. Mater. 26 (2014) 5496–5503.
[6] C. Zhang, Y. Li, C. Ma, Q. Zhang, Small Sci. 2 (2022) 2100086.
[7] T. Shi, R. Wang, Z. Wu, Y. Sun, J. An, Q. Liu, Small Struct. 2 (2021) 2000109.
[8] J.J. Yang, D.B. Strukov, D.R. Stewart, Nat. Nanotechnol. 8 (2013) 13–24.
[9] D. Lee, J. Park, J. Park, J. Woo, E. Cha, S. Lee, K. Moon, J. Song, Y. Koo, H. Hwang, Adv. Mater. 27 (2015) 59–64.
[10] Z. Wang, S. Joshi, S.E. Savel'ev, H. Jiang, R. Midya, P. Lin, M. Hu, N. Ge, J.P. Strachan, Z. Li, Nat. Mater. 16 (2017) 101–108.
[11] Q. Xia, J.J. Yang, Nat. Mater. 18 (2019) 309–323.
[12] Y.C. Bae, A.R. Lee, G.H. Baek, J.B. Chung, T.Y. Kim, J.G. Park, J.P. Hong, Sci. Rep. 5 (2015) 13362.
[13] S. Song, B. Cho, T.W. Kim, Y. Ji, M. Jo, G. Wang, M. Choe, Y.H. Kahng, H. Hwang, T. Lee, Adv. Mater. 22 (2010) 5048–5052.
[14] E. Carlos, R. Branquinho, R. Martins, A. Kiazadeh, E. Fortunato, Adv. Mater. 33 (2021) 2004328.
[15] J. Jang, F. Pan, K. Braam, V. Subramanian, Adv. Mater. 24 (2012) 3573–3576.
[16] C.-R. Cheng, M.-H. Tsai, T.-H. Hsu, M.-J. Li, C.-L. Huang, J. Alloys Compd. 930 (2023) 167487.
[17] G. Tarsoly, J.-Y. Lee, F. Shan, S.-J. Kim, Appl. Surf. Sci. 601 (2022) 154281.
[18] D. Shang, L. Shi, J. Sun, B. Shen, F. Zhuge, R. Li, Y. Zhao, Appl. Phys. Lett. 96 (2010) 072103.
[19] A. Marchewka, B. Roesgen, K. Skaja, H. Du, C.L. Jia, J. Mayer, V. Rana, R. Waser, S. Menzel, Adv. Electron. Mater. 2 (2016) 1500233.
[20] A.R. Patil, T.D. Dongale, R.K. Kamat, K.Y. Rajpure, Mater. Today Commun. 34 (2023) 105356.
[21] S. Lee, T. Kim, B. Jang, W.-Y. Lee, K.C. Song, H.S. Kim, G.Y. Do, S.B. Hwang, S. Chung, J. Jang, IEEE Electron. Device Lett. 39 (2018) 668–671.
[22] J.-H. Park, S.-H. Kim, S.-G. Kim, K. Heo, H.-Y. Yu, ACS Appl. Mater. Interfaces 11 (2019) 9182–9189.
[23] Y.-C. Shen, Y.-C. Shih, Y.-C. Wang, K. Wang, T.-Y. Yang, R.-H. Cyu, Y.-J. Yu, Y.-L. Chueh, ACS Mater. Lett. 3 (2021) 1757–1766.
[24] M.-C. Wu, Y.-W. Lin, W.-Y. Jang, C.-H. Lin, T.-Y. Tseng, IEEE Electron. Device Lett. 32 (2011) 1026–1028.
[25] L. Fu, Y. Li, G. Han, X. Gao, C. Chen, P. Yuan, Microelectron. Eng. 172 (2017) 26–29.
[26] S.-Y. Wang, D.-Y. Lee, T.-Y. Huang, J.-W. Wu, T.-Y. Tseng, Nanotechnology 21 (2010) 495201.
[27] X. Wu, P. Zhou, J. Li, L. Chen, H. Lv, Y. Lin, T. Tang, Appl. Phys. Lett. 90 (2007) 183507.
[28] X. Yan, C. Qin, C. Lu, J. Zhao, R. Zhao, D. Ren, Z. Zhou, H. Wang, J. Wang, L. Zhang, ACS Appl. Mater. Interfaces 11 (2019) 48029–48038.
[29] D. Lee, A.S. Sokolov, B. Ku, Y.-R. Jeon, H.T. Kim, G.H. Kim, C. Choi, Appl. Surf. Sci. 547 (2021) 149140.
[30] M. Ismail, A. Hashmi, A.M. Rana, S. Kim, Nanotechnology 31 (2020) 325201.
[31] Z.-R. Wang, Y.-T. Su, Y. Li, Y.-X. Zhou, T.-J. Chu, K.-C. Chang, T.-C. Chang, T.-M. Tsai, S.M. Sze, X.-S. Miao, IEEE Electron. Device Lett. 38 (2016) 179–182.
[32] D.-C. Hsu, M.-T. Wang, J.Y.-m. Lee, P.-C. Juan, J. Appl. Phys. 101 (2007) 094105.
[33] A. Panca, J. Panidi, H. Faber, S. Stathopoulos, T.D. Anthopoulos, T. Prodromakis, Adv. Funct. Mater. 33 (2023) 2213762.
[34] L. Wang, M.-H. Yoon, G. Lu, Y. Yang, A. Facchetti, T.J. Marks, Nat. Mater. 5 (2006) 893–900.
[35] N. Dehuff, E. Kettenring, D. Hong, H. Chiang, J. Wager, R. Hoffman, C.-H. Park, D. Keszler, J. Appl. Phys. 97 (2005) 064505.
[36] P. Pattanasattayavong, S. Thomas, G. Adamopoulos, M.A. McLachlan, T.D. Anthopoulos, Appl. Phys. Lett. 102 (2013) 163505.
[37] J. Jang, H. Kang, H.C.N. Chakravarthula, V. Subramanian, Adv. Electron. Mater. 1 (2015) 1500086.
[38] B. Jang, T. Kim, S. Lee, W.-Y. Lee, H. Kang, C.S. Cho, J. Jang, IEEE Electron. Device Lett. 39 (2018) 1179–1182.
[39] L. Li, Y. Chen, X. Yin, Y. Song, N. Li, J. Niu, H. Wu, W. Qu, Nanotechnology 28 (2017) 485707.
[40] Y.-H. Kim, J.-S. Heo, T.-H. Kim, S. Park, M.-H. Yoon, J. Kim, M.S. Oh, G.-R. Yi, Y.-Y. Noh, S.K. Park, Nature 489 (2012) 128–132.
[41] S.-J. Park, B.-S. Yu, J.-Y. Jeon, B.-C. Kang, T.-J. Ha, J. Alloys Compd. 825 (2020) 154086.
[42] T. Tang, P. Dacha, K. Haase, J. Kreß, C. Hänisch, J. Perez, Y. Krupskaya, A. Tahn, D. Pohl, S. Schneider, Adv. Funct. Mater. 33 (2023) 2207966.
[43] M.-G. Kim, M.G. Kanatzidis, A. Facchetti, T.J. Marks, Nat. Mater. 10 (2011) 382–388.
[44] D. Spiehl, M. Häming, H.M. Sauer, K. Bonrad, E. Dörsam, IEEE Trans. Electron Devices 62 (2015) 2871–2877.
[45] W. Lee, S. Choi, J. Kim, S.K. Park, Y.H. Kim, Adv. Electron. Mater. 5 (2019) 1900073.
[46] M. Li, J. Zheng, H. Xu, Z. Wang, Q. Wu, B. Huang, H. Zhou, C. Liu, Adv. Mater. Interfaces 5 (2018) 1700981.
[47] Y.S. Rim, H. Chen, Y. Liu, S.-H. Bae, H.J. Kim, Y. Yang, ACS Nano 8 (2014) 9680–9686.
[48] T.B. Daunis, D. Barrera, G. Gutierrez-Heredia, O. Rodriguez-Lopez, J. Wang, W.E. Voit, J.W. Hsu, J. Mater. Res. 33 (2018) 2454–2462.
[49] B. Jang, J. Jang, J.E. Jang, H.-J. Kwon, Ceram. Int. 48 (2022) 20591–20598.
[50] B. Jang, H. Kang, W.-Y. Lee, J.-H. Bae, I.-M. Kang, K. Kim, H.-J. Kwon, J. Jang, IEEE Access 8 (2020) 123013–123018.
[51] S. Petzold, A. Zintler, R. Eilhardt, E. Piros, N. Kaiser, S.U. Sharath, T. Vogel, M. Major, K.P. McKenna, L. Molina-Luna, Adv. Electron. Mater. 5 (2019) 1900484.
[52] H. Zhao, H. Tu, F. Wei, Z. Shi, Y. Xiong, Y. Zhang, J. Du, J. Phys. D-Appl. Phys. 48 (2015) 205104.
[53] K. McKenna, A. Shluger, Appl. Phys. Lett. 95 (2009) 222111.
[54] C.-Y. Li, T.-H. Hsu, C.-L. Huang, J. Alloys Compd. 961 (2023) 170987.
[55] W. Huang, X. Yu, L. Zeng, B. Wang, A. Takai, G. Di Carlo, M.J. Bedzyk, T.J. Marks, A. Facchetti, ACS Appl. Mater. Interfaces 13 (2021) 3445–3453.
[56] S. Ha, H. Lee, W.-Y. Lee, B. Jang, H.-J. Kwon, K. Kim, J. Jang, Electronics (Basel) 8 (2019) 947.
[57] H. Wang, X. Yan, Phys. Status Solidi RRL 13 (2019) 1900073.
[58] D. Kumar, U. Chand, L.W. Siang, T.-Y. Tseng, IEEE Trans. Electron. Devices 67 (2020) 493–498.
[59] J. Zhou, F. Cai, Q. Wang, B. Chen, S. Gaba, W.D. Lu, IEEE Electron. Device Lett. 37 (2016) 404–407.
[60] H. Wan, P. Zhou, L. Ye, Y. Lin, J. Wu, H. Wu, M. Chi, J. Vac. Sci. Technol. B-Nanotechnol. Microelectron. 27 (2009) 2468–2471.
[61] K. Shi, H. Xu, Z. Wang, X. Zhao, W. Liu, J. Ma, Y. Liu, Appl. Phys. Lett. 111 (2017) 223505.
[62] C.-C. Hsu, S.-Y. Hua, X.-Z. Zhang, W.-C. Jhang, C.-W. Cheng, J.-E. Tsai, Y.-M. Wu, Y.-S. Chien, W.-C. Wu, J. Alloys Compd. 898 (2022) 162918.
[63] S. Choi, S.H. Tan, Z. Li, Y. Kim, C. Choi, P.-Y. Chen, H. Yeon, S. Yu, J. Kim, Nat. Mater. 17 (2018) 335–340.
[64] N. Ilyas, J. Wang, C. Li, H. Fu, D. Li, X. Jiang, D. Gu, Y. Jiang, W. Li, J. Mater. Sci. Technol. 97 (2022) 254–263.
[65] J. Lee, J. Park, S. Jung, H. Hwang, in: Proceedings to Joint Conference on IEEE International Interconnect Technology Conference /20th European Workshop on Materials for Advanced Metallization (IITC/MAM), Dresden, Germany, 2011 May 08–12.
[66] K.Y. Shin, Y. Kim, F.V. Antolinez, J.S. Ha, S.S. Lee, J.H. Park, Adv. Electron. Mater. 2 (2016) 1600233.
[67] Q. Xue, Y. Peng, L. Cao, Y. Xia, J. Liang, C.-C. Chen, M. Li, T. Hang, ACS Appl. Mater. Interfaces 14 (2022) 25710–25721.
[68] K.-K. Chiang, J.-S. Chen, J.-J. Wu, ACS Appl. Mater. Interfaces 4 (2012) 4237–4245.
[69] C.-Y. Lin, C.-Y. Wu, C.-Y. Wu, T.-C. Lee, F.-L. Yang, C. Hu, T.-Y. Tseng, IEEE Electron. Device Lett. 28 (2007) 366–368.
[70] H.-T. Tseng, T.-H. Hsu, M.-H. Tsai, C.-Y. Huang, C.-L. Huang, J. Alloys Compd. 899 (2022) 163294.
[71] K.-J. Lee, L.-W. Wang, T.-K. Chiang, Y.-H. Wang, Materials (Basel) 8 (2015) 7191–7198.
[72] U. Rasheed, H. Ryu, C. Mahata, R.M.A. Khalil, M. Imran, A.M. Rana, F. Kousar, B. Kim, Y. Kim, S. Cho, J. Alloys Compd. 877 (2021) 160204.
[73] K.P. Biju, X. Liu, M. Siddik, S. Kim, J. Shin, I. Kim, A. Ignatiev, H. Hwang, J. Appl. Phys. 110 (2011) 064505.